Educational Administration: Theory and Practice
2025, 31(1), 485 - 499
ISSN: 2148-2403
https://kuey.net/

Research Article

Numerical simulation of thermomechanical stresses during thermal fatigue tests with a view to predicting its duration

Achegaf Zineb*

*LabSTIC Laboratory, Abdelmalek Essaadi university, National School of Applied Sciences,BP 2222, Tetouan 93000, Morocco
zachegaf@uae.ac.ma

Citation: Achegaf Zineb (2025), Numerical simulation of thermomechanical stresses during thermal fatigue tests with a view to predicting its duration, *Educational Administration: Theory and Practice. 31(1), 485 - 499*
Doi: 10.53555/kuey.v31i1.9541

ARTICLE INFO

ABSTRACT

This article focuses on the analysis of thermomechanical stresses undergone by a sample during FT tests in order to predict its service life, particularly from the angle of crack propagation. This is indeed an essential complement to metallurgical analyses for the study of steel damage by FT. We present in this article the methodology pursued for analytical and numerical calculations. The approach consisted first of all in determining the thermal stresses, then mechanical stresses, via finite element structure calculations. The numerical simulation is carried out by the Finite Element Method (FEM) under ABAQUS™ in implicit resolution, using the Thermo-Elasto-Plastic (EP) and Thermo-Elasto-Visco-Plastic EVP behavior laws. The axisymmetry of the reduced specimen "SR1" (1 mm thick, geometry of revolution) and the thermal stresses makes it possible to treat the problem in two dimensions. The calculation is therefore carried out on a quarter of the meridian section of the FT specimen. The results of the numerical simulation were then used in an analysis based on fracture mechanics in order to study the cracking kinetics under transient thermal loadings.

Keywords: Tool steels, thermal fatigue FT, oxidation, crack initiation, crack propagation, stress intensity factor FIC, crack opening.

2. Introduction

Thermal Fatigue (FT) is a process of gradual deterioration of materials stressed by repeated heating and cooling cycles, while their thermal expansion or contraction is partially or completely hindered [22]. The material is then subjected to transient thermomechanical stresses that can induce inelastic deformations. We speak more specifically of Thermomechanical Fatigue (TMF), when the restriction is imposed on the thermal deformation of the material by external forces applied to its free surfaces [22, 23]. In our case, we are only interested in thermal fatigue, in which the stresses are exclusively of internal origin (material). This case of fatigue concerns parts presenting anisotropic thermal expansions due to thermal gradients resulting from heating or cooling. The restraint is called "internal" because the expansion or contraction of each isothermal set of elements of the structure is prevented by the set of adjacent elements, of different temperature, which makes the FT a structural problem.

3. Numerical simulation of thermal and mechanical (or thermomechanical) stresses

3.1. Meshing of the specimen

The mesh is created under IDEAS™ and then exported to ABAQUS™. It is composed of quadratic (rectangular) axisymmetric elements with 8 nodes of the following type: “DCAX8” (Diffusive Heat Transfer Elements) with linear interpolation, for thermal calculation, “CAX8” (Strain Displacement Elements) with bilinear interpolation, for mechanical calculation.

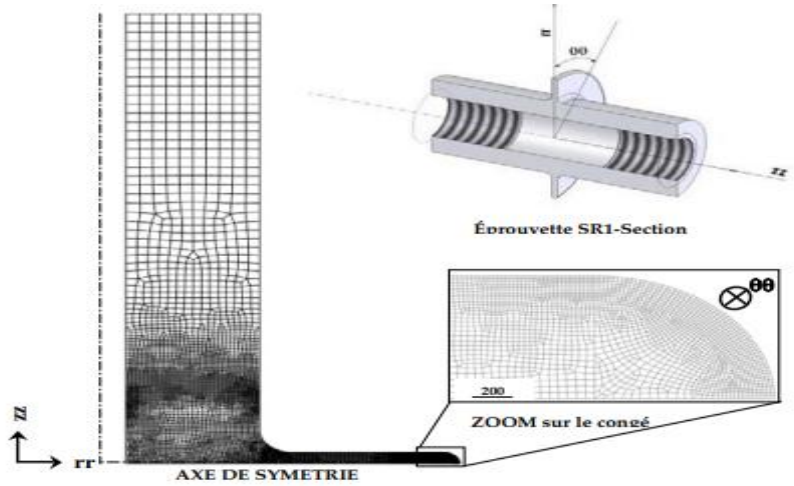

Figure 1: Mesh of the quarter of the cross-section of the "SR1" specimen (IDEAS™)

The thermal calculation consists of solving the heat equation which is written in the following form:

$$div\left(\lambda\overrightarrow{grad}T\right)-C_p\rho\frac{\partial T}{\partial t}=-P \qquad \textbf{(1)}$$

where: λ , ρ and Cp are respectively the thermal conductivity, density and specific heat (heat capacity) of the medium, T is the temperature, t is the time and P is a power (source term).

For the homogeneous and isotropic medium with thermo-physical characteristics dependent on the temperature and in axisymmetric conditions, the heat equation is then reduced to [6]:

$$\rho(T)C_p(T)\frac{\partial T(r,z,t)}{\partial t}=\lambda(T)\left(\frac{1}{r}\frac{\partial}{\partial r}\left(r\frac{\partial T(r,z,t)}{\partial r}\right)+\left(\frac{\partial^2 T(r,z,t)}{\partial z^2}\right)\right) \qquad \textbf{(2)}$$

Equation (2) is solved numerically by the FEM from the initial and boundary conditions

The temperature readings by the thermocouples during the different cycles studied are presented in Figure 2.

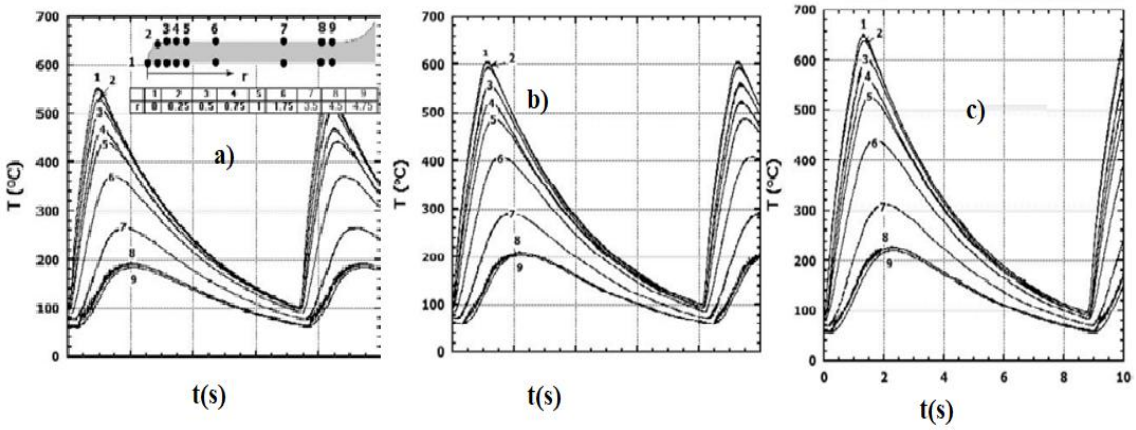

Figure 2: Thermal evolutions measured at different depths during the FT cycle a), b) and c) respectively at Tmax = 550, 600 and 650 °C

- **Initial and boundary thermal conditions**

Initially the structure is at 20 °C : A t=0 $\forall M\in\Omega : T(r,z,0)=T_0=20°C$ **(3)**

- Heating heat flow (Neumann conditions):

For $M\in\partial\Omega_{ch}$: $r\in[14.5,15], z\in[0,0.5]$; $-\lambda(T)\left(\frac{\partial T(r,z,t)}{\partial r}+\frac{\partial T(r,z,t)}{\partial z}\right)=\varphi(t)$ **(4)**

- Cooling heat flow : For $M\in\partial\Omega_{ext}$: $r\in[9,15], z\in[0,20]$

$$-\lambda(T)\left(\frac{\partial T(r,z,t)}{\partial r}+\frac{\partial T(r,z,t)}{\partial z}\right)=B[T^4(r,z,t)-T_{air}^4]+h_{air}\left[T(r,z,t)\_T_{air}\right] \quad \textbf{(5)}$$

And for $M\in\partial\Omega_{\text{int}}$: $r=5, z\in[0,20]$; $-\lambda(T)\left[\frac{\partial T(r,z,t)}{\partial r}\right]=h_{eau}\left[T(r,z,t)\_T_{film}\right]$ **(6)**

➢ Mechanical boundary conditions

The resolution of the thermomechanical problem is based on the equilibrium equations relating to the mechanical boundary conditions as well as on the behavior law.

The equilibrium equation and the mechanical boundary conditions (figure 4) are written as follows:

$$\forall M\in\Omega, \overrightarrow{div}\left(\overset{\Rightarrow}{\sigma}\right)=\vec{0}\text{, avec : } \vec{U}\cdot\vec{e}_{zz}=0 \text{ pour } M\in\partial\Omega_{sym} : r\in[5,15], z=0 \quad \textbf{(7)}$$

Where $\overset{\Rightarrow}{\sigma}$ is the Cauchy stress tensor

Figure 3 illustrates the fields of application of each heat exchange. The air convection φ_{cl} and radiation cooling flows φ_r occur across the external boundary ($\partial\Omega_{ext}$), and that by forced convection φ_{cf} occurs on the internal wall $\partial\Omega_{\text{int}}$

The heat flux density (in W.m^{-2}) along a direction characterized by the normal vector $\vec{n}$ to the surface (S) crossed by the flow is given by Fourier's law [18]:

$$\varphi=\vec{j}\vec{n}=-\lambda(T)\overrightarrow{gradT}\vec{n} \quad \textbf{(8)}$$

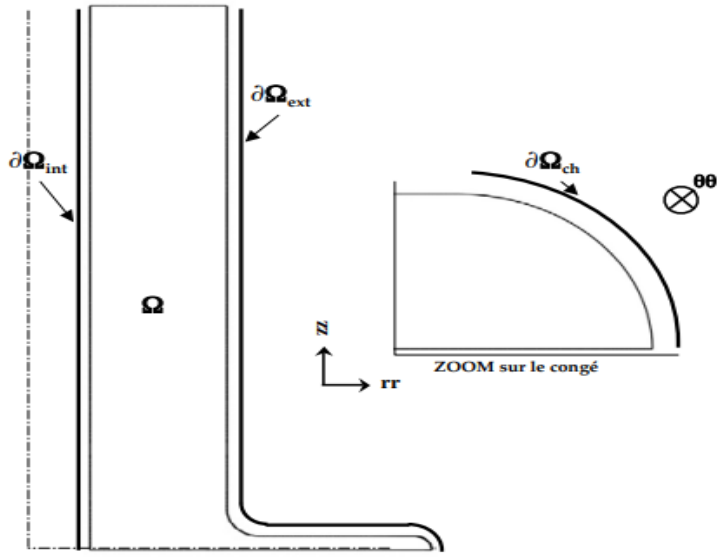

Figure 3: Boundaries of application of heat exchange flows

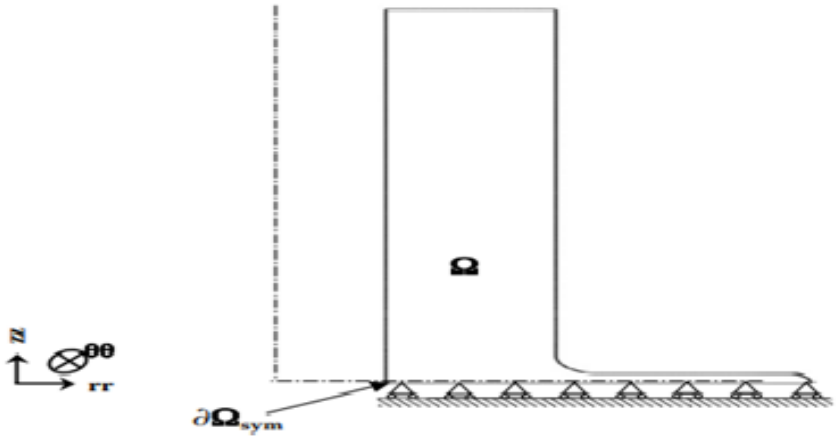

Figure 4: Mechanical boundary conditions

➢ Determination of the heating heat flow

The determination of the heat flow can be done easily in the case of a plate or a cylinder [19.8].
In the case of a tubular cylinder in X38CrMoV5 stressed under conditions similar to our tests:

$$\phi_{cylindre} = 2\pi RZ\varphi_{cylindre} \quad \textbf{(9)}$$

Where R and Z are respectively the outer radius of the cylinder (15 mm) and the slice width (0.5 mm) .

$$\varphi_{disque} = \phi_{cylindre} / S_{congé} \text{ and } S_{congé} = \left(\pi/2\right) r.2\pi\left(R-r\right) \quad \textbf{(10)}$$

Here, R and r are respectively the radius of the specimen (radius of the disk) and the fillet.

➢ Determination of cooling thermal flows

The densities of cooling thermal flows can be modeled by a linearized law of the type:

$$\varphi(t) = h[T(M,t) - T_{ext-c}] \quad \textbf{(11)}$$

Where $T(M,t)$ is the temperature of a point on the boundary considered at a given time, φ is the density of the heat flux, h is the heat exchange coefficient with the external source and T_{ext-c} is a characteristic temperature of the external environment. We then write:

$$\varphi_r = h_r[T_M - T_{ext-c}] = B[T_M^4 - T_{air}^4] \text{ with } B = \sigma\varepsilon_M F_M \quad \textbf{(12)}$$

$$\varphi_{cl} = h_{air}\left[T_M \_ T_{air}\right] \quad \textbf{(13)}$$

$$\varphi_{cf} = h_{eau}\left[T_M \_ T_{film}\right] \quad \textbf{(14)}$$

Where σ is the Stefan-Boltzmann constant, ε_M is the emissivity of steel, F_M is a form factor, T_M is the temperature of a point M on the exchange surface, T_{air} is the air temperature, T_{film} is the temperature of the viscous film where the exchange between the internal wall and the water takes place and h_r , h_{air} and h_{eau} are respectively the heat exchange coefficients by radiation, free air convection and forced convection with water [8,10]. The parameters related to heat exchanges used in the calculation are presented in Table 1.

σ (W.m^{-2}.K^{-4})	ε_M	T_{air} (K)	T_{eau} (K)	T_{film} (K)	h_{air} (W.m^{-2}.K^{-1})	h_{eau} (W.m^{-2}.K^{-4})
5,67 10^{-8}	0,88	293	293		20	7000

Table 1: Data used in thermal calculation

3.2. Numerical simulation of thermomechanical effects

Thermomechanical loads are calculated from the results of the thermal calculation and the thermomechanical properties of the material [13,14,15,16,65].

➢ Elasto-Plastic (EP) behavior model

In this case, the behavior of the material is assumed to be elasto-plastic (EP) and the work hardening (Figure 5) is isotropic [3,4] at different temperatures defined by a Ramberg-Osgood type law described by the following relations: $\varepsilon(\sigma,T) = \dfrac{\sigma}{E(T)} + \left(\dfrac{\sigma}{K(T)}\right)^{M(T)}$ **(15)**

With $\varepsilon_{tot}(T) = \varepsilon_{el}(T) + \varepsilon_{in}(T)$ and $\varepsilon_{el}(\sigma,T) = \dfrac{\sigma}{E(T)}$ Where ε_{tot}, ε_{in} and ε_{el} are respectively the total true, inelastic (plastic) and elastic strains, σ is the true stress and E, K and M are temperature-dependent material parameters.

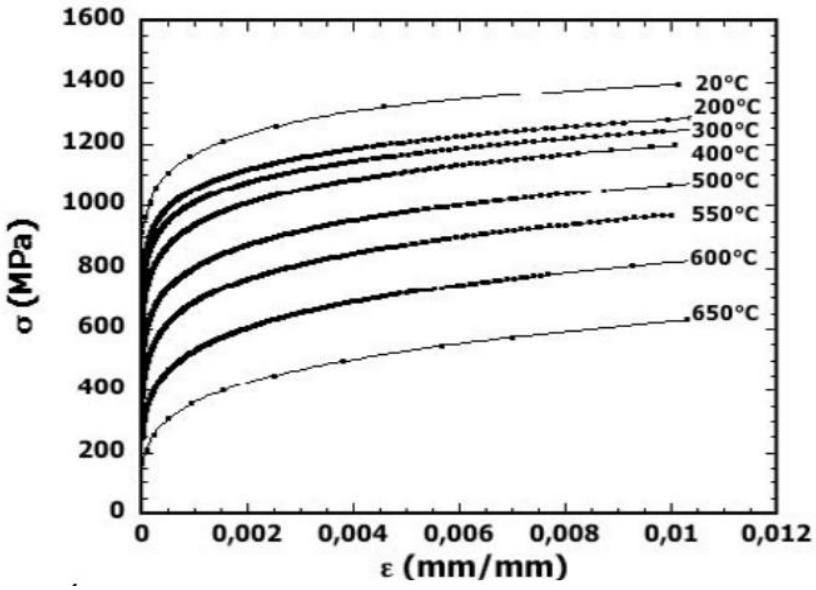

Figure 5: Evolutions of inelastic deformation with stress at different temperatures described by the Romberg-Osgood law from simple tensile tests

➢ Elasto-Visco-Plastic (EVP) behavior model

We now report the simplified form of the model in 1D (one-dimensional) [4,5,6,9,11]. The expression of the model according to the isotropic and kinematic component is given in Table 2.

Load surface	**Composante cinématique**	**Isotropic component**
	$f = \left\lvert \sigma - \sum_{i=1}^{2} X_i \right\rvert - R^s$	$f = \left\lvert \sigma - \sum_{i=1}^{2} X_i \right\rvert - \sum_{i=1}^{2} R_i - R_0$
State laws: for i=1,2	$X_i = C_i \alpha_i$	$\sigma = E\varepsilon_{el}$ $X_i = C_i \alpha_i$ **and** $R_i = b_i Q_i r_i$
	With $\varepsilon = \varepsilon_{el} + \varepsilon_{vp}$	
Laws of evolution: for i=1.2	$\dot{\alpha}_i = \dot{\varepsilon}_{vp} - D_i \dot{p} \alpha_i$	$\dot{\alpha}_i = \dot{\varepsilon}_{vp} - D_i \dot{p} \alpha_i$ **et** $\dot{r}_i = \dot{p}\left(1 - b_i r_i\right)$
Viscoplastic flow law (Norton's law)	$\left\lvert \dot{\varepsilon}_{vp} \right\rvert = \dot{p}$; $\dot{p} = \left\langle \frac{f}{K} \right\rangle^n$	

Table 2: One-dimensional description of the EVP model [4]

Where, ri and α_i are internal variables of the isotropic and kinematic component, Xi and R_{1-2} ar respectively

the of kinematic and isotropic hardening variables, R_o and R^S are respectively the initial true elastic limit and the stabilized cycle, p is the cumulative plastic strain, ε_{vp} is the viscoplastic strain and Ci ,Di ,Qi and bi : are material parameters, depending on the temperature.

Table 3 shows the values retained for the different temperatures, for each of the twelve parameters of the model. The thermomechanical stresses are calculated by implementing these coefficients in 3D (multiaxial formalism) in ABAQUS™, via the external library Zmat [4,20,21].

Component of the EVP model		T (°C)						
		20	200	300	400	500	600	650
	$E\left(GPa\right)$	204	195	187	179	165	147	127
	$R_0\left(MPa\right)$	715	685	610	562	525	505	390
	Q_1	-78,5	-90	-95	-100	-160	-210	-173
	b_1	0,3	0,3	0,3	0,3	0,3	0,3	0,5
	Q_2	-205	-183,5	-79,5	-53	-91	-150	-143
	b_2	15	9 ,7	5 ,6	5	4,9	4	5,5
	K	100	110	120	200	350	455	484
	n	18,5	16,5	13,5	10,5	8,0	6,0	7,99

	C_1	830000	805560	771420	730000	690000	599600	454000
	D_1	5000	5000	5000	5000	5000	5000	19697
	C_2	300110	271650	232310	190740	150630	55320	61911
	D_2	500	500	500	500	500	500	816
E , R_0		Young's modulus and initial true elastic limit						
K, n		Viscosity coefficients						
C_1, C_2		Terms of the kinematic law						
D_1, D_2		Dynamic recovery terms						
Q_1, Q_2, b_1, b_2		Terms of the isotropic law						

Table 3: EVP model coefficients identified for X38CrMoV5 47 HRC [4,6,7]

4. Calculation results

4.1. Thermal calculations

Figure 6 illustrates the variations of T_{min} and T_{max} calculated at the node located in position "1", during the first five cycles of the numerical simulation. A stabilization of the thermal cycle is noted from the first cycle

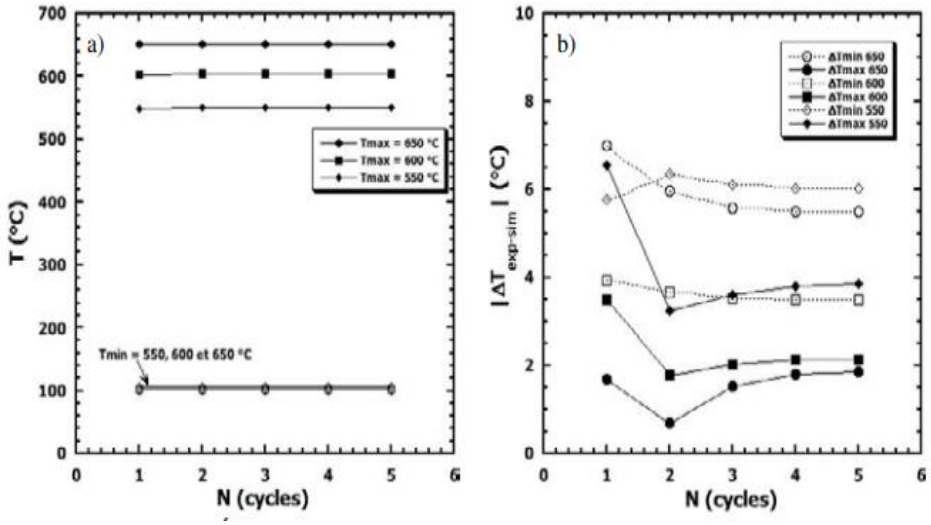

Figure 6: Evolution of T_{max} and T_{min} during 5 numerical simulation cycles a) Evolution of Tmin and Tmax, b) Variation of thermal differences, in absolute value, between the numerical simulation and the experiment

The absence of a transition regime preceding the stabilization of the thermal cycles can be explained by the application of preheating and by the reduced dimensions of the specimen, which makes it possible to establish a thermal gradient in steady state equal to that of the beginning of the FT cycle. It is also noted that the variation of the difference between the measurement and the calculation of Tmin and Tmax stabilizes from the third cycle (Figure 6.b). The correlation between the calculated and measured temperatures is also convincing in depth, although a slight difference is observed at the end of cooling (Figure 7.a,c and e).

The depth distributions of T_{min} and T_{max} as well as the thermal gradients caused during the different thermal cycles are presented in Figure 7.b, d and f.

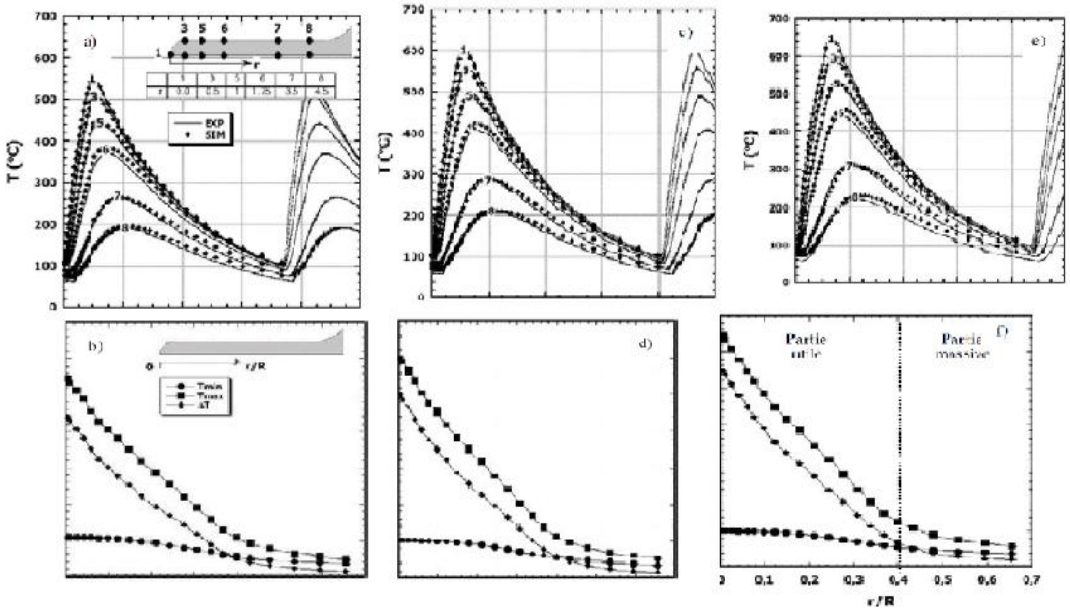

Figure 7: Thermal maps (temporal evolutions of temperature at different depths; thermal gradient profiles and temperature minima and maxima) a,b) $T_{max} = 550°C$ **, c,b)** $T_{max} = 600°C$ **and e,f)**

Figure 8 illustrates the variation of thermal differences between nodes located at the same depth along the "rr" axis on the external surface of the disk and on the plane of symmetry ("z=0").

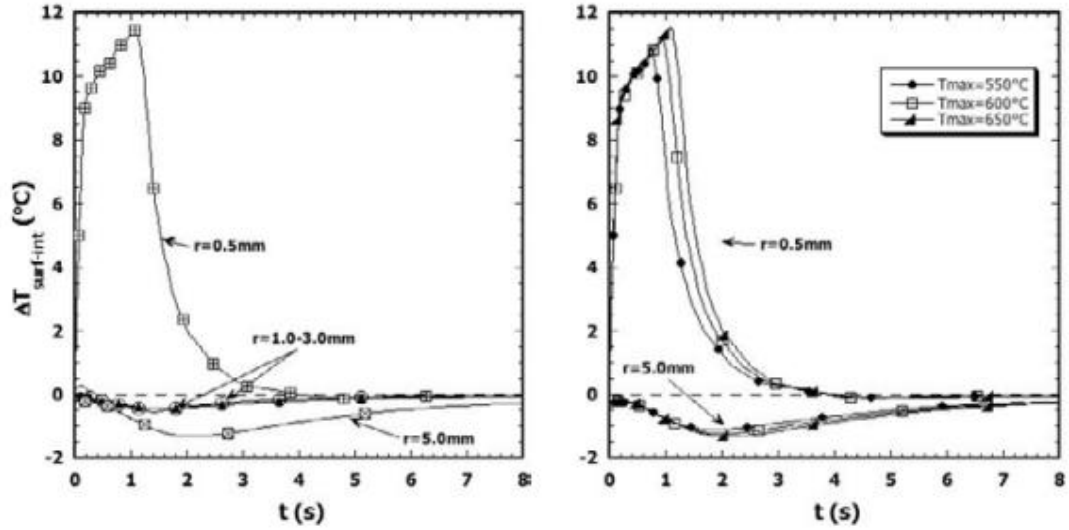

Figure 8: Variation of the temperature difference between the core and the surface of the disk

a) $T_{max} = 650°C$ **for r = 0.5 – 5.0 mm, b)** $T_{max} = 550 - 650°C$ **for r= 0.5 and 5 mm**

4.2. Mechanical calculations

The thermomechanical calculation, for each T_{max} and behavior law used, was conducted on five thermal cycles in addition to the preheating part. The calculation is performed by applying the consecutive thermal cycles obtained by the numerical simulation.
The thermomechanical quantities sought are listed in Table 4

Stress (MPa)	deformation in (mm/mm)				
	Total	Thermal	Mechanical	Elastic	Inelastic
σ	$\varepsilon_{tot}(T)=\varepsilon_{mec}(T)+\varepsilon_{th}(T)$ **(16)**	$\varepsilon_{th}(T)=\alpha(T)(T-T_{ref})$ **(17)**	ε_{mec}	**Loi de Hooke** $\varepsilon_{el}(T)=\frac{\sigma}{E(T)}$ **(18)**	ε_{in}

Table 4: Notation of mechanical quantities extracted from calculations

Where $\alpha(T)$ is the coefficient of thermal expansion (expansion coefficient) and T_{ref} is the reference temperature corresponding to the initial temperature (20 °C).
Thermal deformation results from the expansion or contraction due to the increase or decrease in the temperature of the element.
Mechanical deformation includes an elastic ε_{el} and inelastic ε_{in} component according tothe equation :

$$\varepsilon_{mec}(T)=\varepsilon_{el}(T)+\varepsilon_{in}(T) \quad \textbf{(19)}$$

➢ Evolution of thermal, total and mechanical deformations

The deformations are in fact greater in the hottest part of the specimen, where the highest thermal gradients are located. Thus, the analysis of the results is done beforehand for the extreme part of the specimen (Point 1).
The thermal deformations given by the calculations using the EP and EVP laws are identical, because the same thermal expansion coefficients are used in both cases. It is also noted that the mechanical cycles, like the thermal stress, stabilize from the first cycle. Figure 9 showed that the evolution of thermal deformation follows a single curve regardless of Tmax, while the amplitude of thermal expansion depends on the maximum temperature level. The asymmetry of the thermal cycle causes a shift between the evolution curves of the total and mechanical deformation during the increase and decrease in temperature (see Figure 9.c and e).
The thermal, total and mechanical deformations imposed on the end of the specimen during the fifth cycle are given in Table 5.

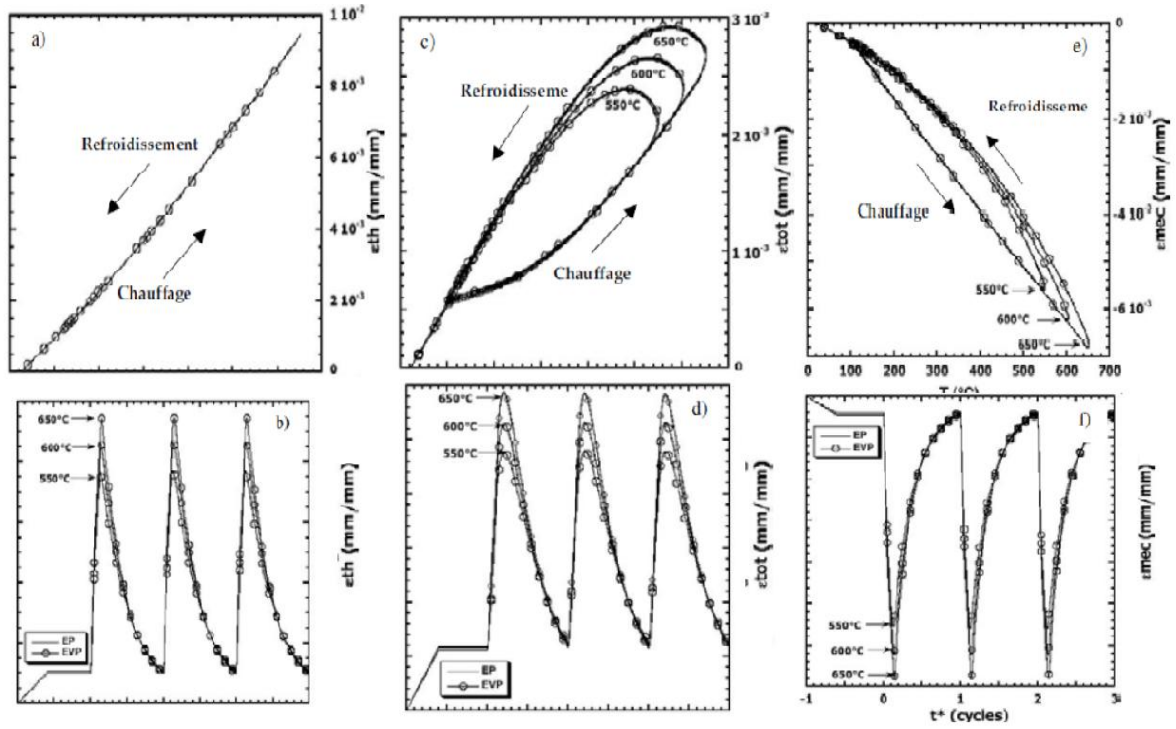

Figure 9: Evolutions as a function of temperature and time (calculated at point 1 of the disk for the different T_{max} : Thermal expansion (a and b), Total deformation (c and d) Mechanical deformation (e and f)

T_{max} (°C)	ε_{th} min	ε_{th} max	$\Delta\varepsilon_{th}$	ε_{tot} min	ε_{tot} max	$\Delta\varepsilon_{tot}$	ε_{mec} min	ε_{mec} max	$\lvert\Delta\varepsilon_{max}\rvert$
550	10,5 e^{-4}	7,69 e^{-3}	6 ,63 e^{-3}	6,1 e^{-4}	2,39 e^{-3}	1,77 e^{-3}	-5,60 e^{-3}	-4,4 e^{-4}	5,16 e^{-3}
600	9,9 e^{-4}	8,60 e^{-3}	7,60 e^{-3}	5,7 e^{-4}	2,65 e^{-3}	2,07 e^{-3}	-6,24 e^{-3}	-4,1 e^{-4}	5,82 e^{-3}
650	9,6e^{-4}	9,43 e^{-3}	8,47 e^{-3}	5,7 e^{-4}	2,91 e^{-3}	2,33 e^{-3}	-6,80 e^{-3}	-3,9 e^{-4}	6,41 e^{-3}

Table 5: Calculated thermal, total and mechanical deformation at the extremity of the specimen for different T_{max}

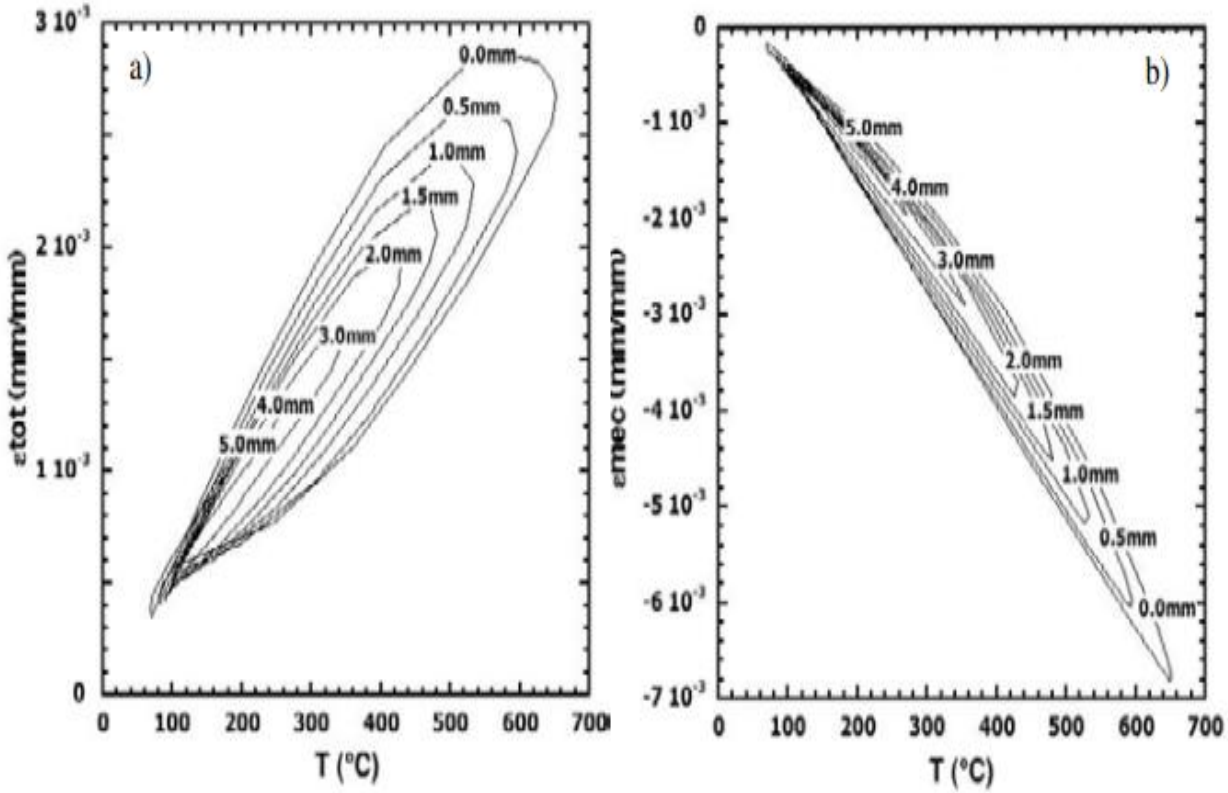

Figure 10: Evolution during the stabilized cycle for Tmax = 650 °C of the total deformation (a) and the mechanical deformation (b) as a function of the temperature at different depths of the disk

The total and mechanical deformation loops at different depths of the disk are shown in Figure 10. These results are from the EP calculation at the stabilized cycle for $T_{max} = 650°C$. As the depth increases, the amplitude of the total deformation decreases with the temperature levels. The mechanical deformation remains negative (compression) in the disk but with decreasing amplitudes with depth. Indeed, the central part of the specimen is less hot than the disk, which is subject to compression deformations due to the prevention of its expansion relative to the barrel of the specimen.

➢ Stress evolution

An example of the stress evolution calculated with the EP model is illustrated in Figure 11 a and b [2].

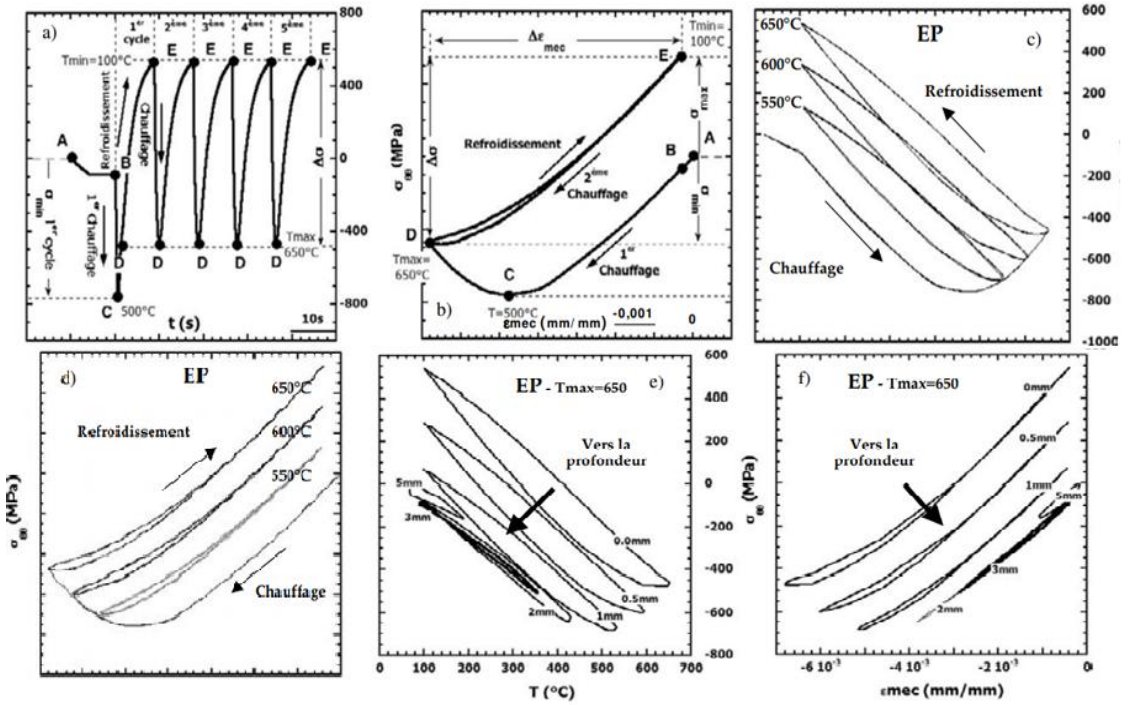

Figure 11: Evolution of stress as a function of temperature (or time) and mechanical deformation, calculated with the EP model for the different T_{max} a-d) at the end of the specimen, e) and f) at the depth of the disk

The letters A, B, C, D and E mark the specific events during the FT test. At the starting point A (rest), the stress (of thermal origin) and the corresponding deformations are zero. The thermal gradient resulting from preheating causes the surface maintained at 100 °C to undergo elastic compression (B). During the first heating (BD), the stress evolves into compression in thermoelasticity up to point C, where the peak of the minimum stress is recorded at around 500 °C for a mechanical deformation of the order of $\varepsilon_{mec} = -4.0e^{-3} mm/mm$. Above this point, an inelastic deformation is initiated. Indeed, the mechanical properties of steel, in particular its elastic limit, decrease considerably beyond this temperature, thus leading to a drop (in absolute value) in the compressive stress accompanied by an increase in the amplitude of the plastic deformation (CD). This explains the phase shift between the maximum temperature and the peak of the maximum stress during the first FT cycle, which is a direct consequence of the choice of the position of the starting point (A). During cooling (DE), the stress is thermoelastically discharged following a path parallel to (AC). At the end of cooling, the end of the specimen is under tension due to the discharge of the negative stress developed during heating. The minimum temperature and the maximum tensile stress coincide at point E, with a non-zero residual mechanical strain (preheating strain).

During the following cycle, the stress travels, back and forth in the case of the EP calculation, the ED path. During heating, the stress decreases in order to discharge the tension developed at the end of the previous cooling, then continues to evolve in compression to reach its threshold at T_{max}. Figure 11.c and d show the stress evolutions as a function of temperature and mechanical strain for the three T_{max} studied. The stress variation is similar to that of the strain for the three T_{max}, which are differentiated by the levels of minimum stresses and thus by the tensile stress. The latter increases with the rise in maximum temperature as does the average stress $\sigma_{moy} = 0.5*(\sigma_{max} + \sigma_{min})$ and the stress amplitude ($\Delta\sigma = \sigma_{max} - \sigma_{min}$). Indeed, during the first heating, the stress exceeds the flow limit of the material from point C (500 °C). Above this temperature, the stress decreases because the mechanical properties of the steel drop in accordance with the isothermal tensile curves illustrated in Figure IV.8. However, it is at the lowest test temperatures that the highest compressive stresses are recorded (section CD). The same phenomenon is observed within the specimen tested for the same T_{max} (the decrease in temperature at depth is accompanied by an increase in the compressive stress in the fillet). Figure 11.e and f show as an example the evolution of the mechanical hysteresis loops (stress-temperature and stress-strain) at depth for the EP calculation at $T_{max} = 650°C$. As we can see, the compressive stress levels increase in the first millimeter then decrease to zero around the sixth millimeter. The tension which is a consequence of the thermo-elastic unloading decreases for this

purpose, leading to the displacement of the loops at depth. The results of the calculations (EP and EVP) of the stress at the end of the specimen at the fifth cycle and for the three T_{max} are grouped in Table 6. The extreme surface of the specimen is therefore subjected to compression-traction stress cycles while the mechanical deformation cycles are compression-compression cycles. The results of the calculation using the EVP model differ from those from the EP calculation by the stress levels and by the evolution of the latter over time, although the stress amplitudes ($\Delta\sigma$) are close in both cases.

$T_{max} = 550°C$			$T_{max} = 600°C$			$T_{max} = 650°C$			
$\sigma_{\theta\theta}$ min	$\sigma_{\theta\theta}$ max	$\sigma_{\theta\theta}$ min	$\sigma_{\theta\theta}$ min	$\sigma_{\theta\theta}$ max	$\sigma_{\theta\theta}$ min	$\sigma_{\theta\theta}$ min	$\sigma_{\theta\theta}$ max	$\sigma_{\theta\theta}$ min	
-698	133	832	-597	339	936	-478	539	1018	EP
-796	27	823	-773	117	890	-621	399	1021	EVP

Table 6: Stresses generated at the end of the specimen, given by the EP and EVP calculation after 5 cycles (value in MPa)

➢ Evolution of the inelastic deformation

The most significant inelastic deformation is generated at the first heating, starting at 360°C.
In the second cycle, the calculation using the EP model gives an inelastic deformation of very low amplitude which is cancelled at the following cycles (3-5 cycles) (see Figure 12). With the EVP model, the inelastic deformations persist throughout the five cycles, but with decreasing amplitudes. Part of the cyclic inelastic deformation is restored (inelastic deformation in tension) at the end of heating for the thermal cycle at $T_{max} = 650°C$ (Figure 12.f).

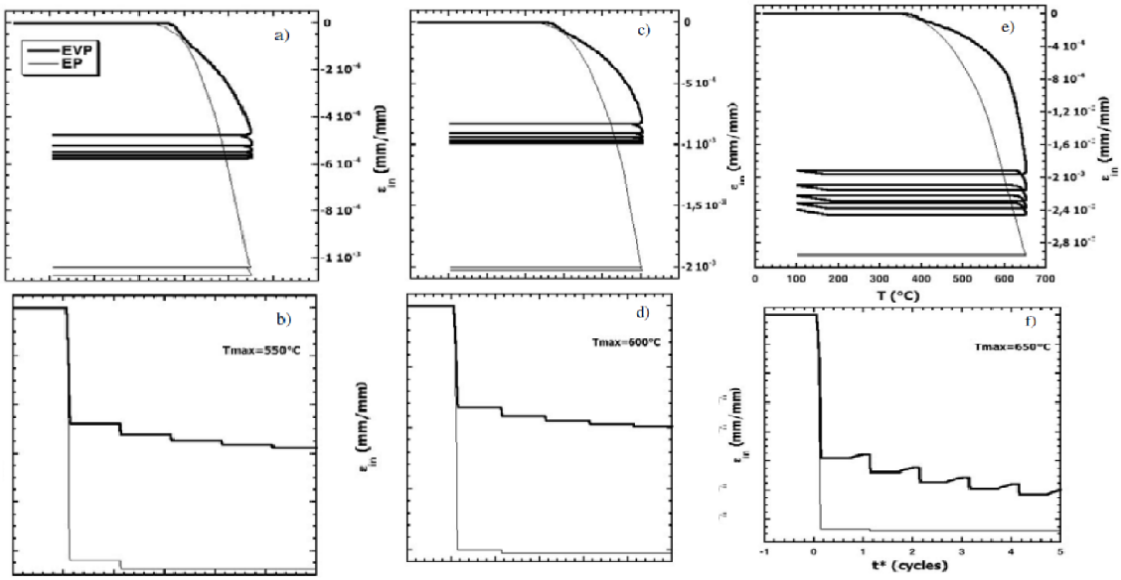

Figure 12: Evolution of the inelastic deformation at the end of the specimen over time (5 cycles) and as a function of temperature, calculated by the EP and EVP model. a,b) $T_{max} = 550°C$ **, c,b)** $T_{max} = 600°C$ **and e,f)** $T_{max} = 650°C$ **.**

The EP and EVP calculation results of the inelastic deformation and the amplitudes of the total plastic deformation during the five cycles are given in Table 7. It is noted that the two models agree in showing that after five cycles the amplitude of the total inelastic deformation at $T_{max} = 550°C$ was doubled, then tripled successively, for the maximum temperatures 600 and 650 °C.

Law of behavior	$T_{max} = 550°C$		$T_{max} = 600°C$		$T_{max} = 650°C$	
	ε_{in} min	$\Delta\varepsilon_{in}$	ε_{in} min	$\Delta\varepsilon_{in}$	ε_{in} min	$\Delta\varepsilon_{in}$
EP	-1,073 e^{-3}	-1,073 e^{-3}	-2,026 e^{-3}	-2,026 e^{-3}	-2.944 e^{-3}	-2.944 e^{-3}
EVP	-5,743 e^{-4}	-5,620 e^{-4}	-9,686 e^{-4}	-9,895 e^{-4}	-2,268 e^{-3}	-2,401 e^{-3}

Table 7: Inelastic deformations produced in the end of the specimen, given by the EP and EVP models after 5 cycles (values in mm/mm

➢ Effect of the behavior law

The EP and EVP models are distinguished by the description of the material behavior response in cyclic plasticity and its evolution [1,8,3]. As shown in Table 6 and Figure 12, for the same thermal stress conditions (equal imposed mechanical deformations), the two models give very different inelastic deformation amplitudes, especially during the first heating. The levels of tension and compression stresses, and also for the mean stress, are therefore different.

The mechanical stress-strain hysteresis loops stabilize from the second cycle in the EP calculation where the hardening is considered isotropic, while they do not stabilize in the case of the EVP model. To better illustrate the difference between the two models, the evolutions of the stress at the extremity of the experiment as a function of the mechanical and inelastic deformation for the three T_{max} are plotted in the same curves (Figure 13).

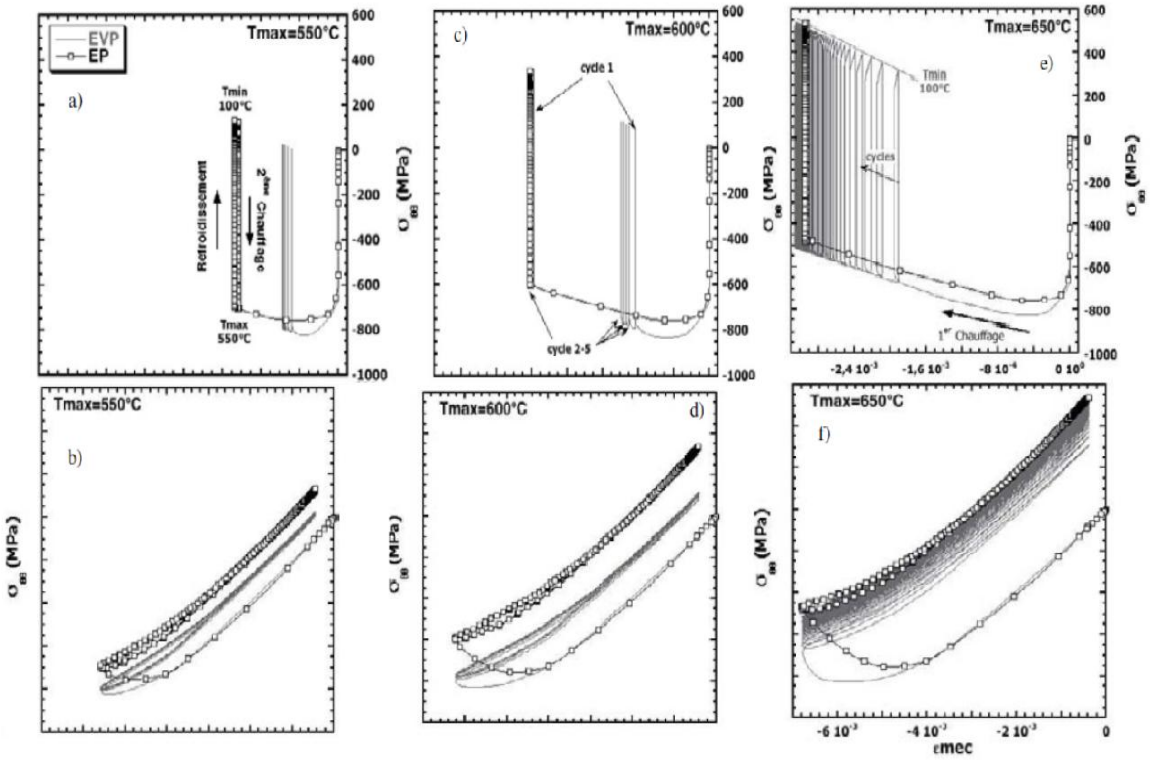

Figure 13: Evolution of the stress calculated by the EP and EVP model at the extremity of the specimen, as a function of the inelastic and mechanical deformation

If the EVP model shows less plasticity in this part, this is because it takes into account the effects related to the strain rates.

The variation of the mechanical strain as a function of time during heating and cooling for the different T_{max} and the strain rates determined on the segments presenting a linear evolution are shown in Figure 14. The rates are generally less significant during cooling, although the rates are symmetrical at the beginning of this stage and at the end of heating. The average rate in the FT tests is a hundred times greater than that used in the tensile tests used to identify the EP model parameters. However, it is known that the behavior of X38CrMoV5 steel is sensitive to the test frequency, particularly when hot [3]. The stresses increase while the plastic deformation decreases for the fastest stresses (see Figure 15).

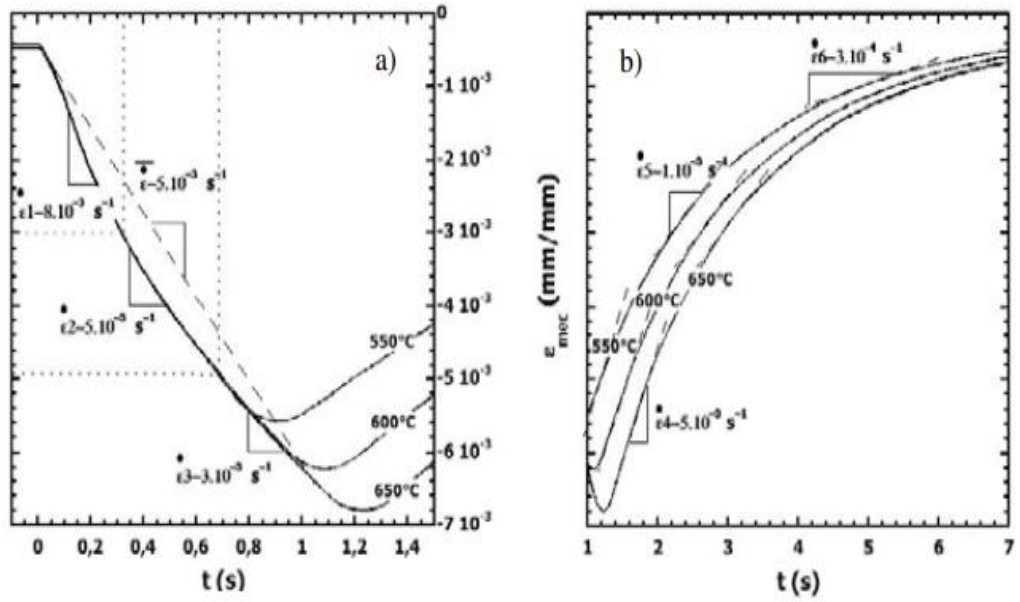

Figure 14: Evolution of mechanical deformation rates during FT tests: a) Heating period and b) Cooling period

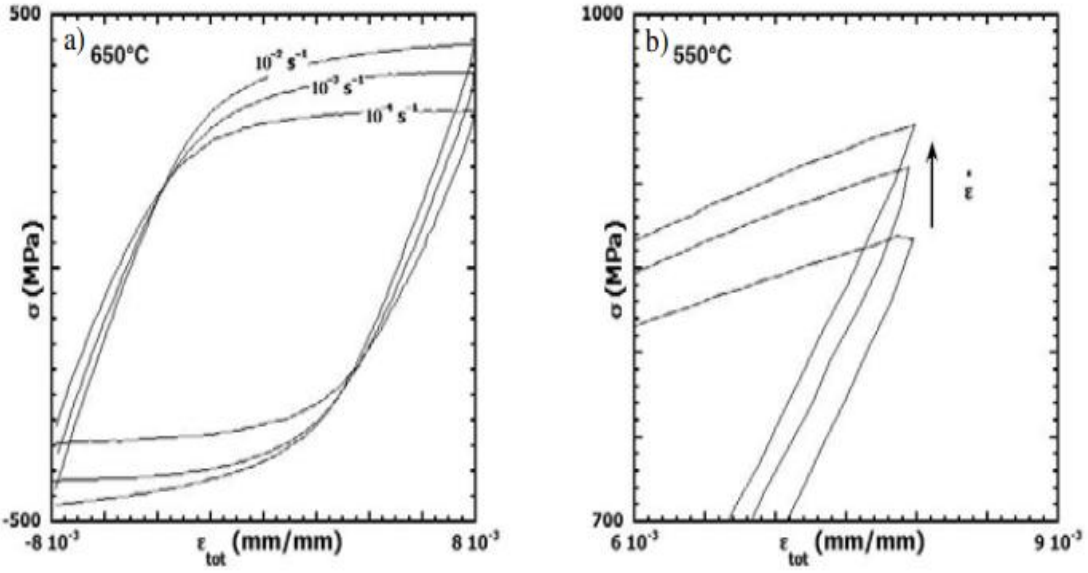

Figure 15: Mechanical hysteresis loops (stress-strain) obtained at stabilized cycle in FI at different test frequencies [1]: a) T = 650 °C and b) T= 550 °C

Monotonic or cyclic isotropic hardening of materials is well taken into account by both models, but in very different ways. In the EP calculation, this phenomenon manifests itself by a hardening. Indeed, after the first plasticization, the EP model gives, for an equal stress, a very low inelastic deformation in the second cycle. This deformation remains unchanged (almost zero) in the following cycles (Figure 13.a, c and e). On the other hand, the EVP model shows a cyclic softening and presents an evolution of the average stress thus moving the hysteresis loops towards increasingly higher stresses. An EP model with isotropic hardening could be used to analyze the thermomechanical stresses of an FT test when the amplitude of the plastic deformation is low [8,12].

5. Conclusion

The Temperature, Stress and Strain fields as a function of time (TCDt) were determined in the case of the "SR1" specimen for the different thermal conditions studied. The thermal maps as well as the evolutions of the heat fluxes recorded experimentally were used for the validation of the thermal calculation. Two elasto-plastic and elasto-visco-plastic behavior models were used in the thermomechanical calculation. Due to the calculation time, the numerical simulation was howevesr limited to a few dozen cycles.

It turns out that, independently of the behavior law used and the temperature conditions, the external surface of the specimen always remains in compressive deformation while the stress cycle is in the compression-traction phase (heating-cooling). The compressive stresses for the three maximum temperatures are comparable, but the tensile stresses, generated at the end of cooling, are all the more important as the maximum temperature of the cycle is higher. This difference is due to the plastic deformation accumulated during the first heating and restored during cooling.

The results of the mechanical calculations show that the variation of the stress ($\Delta\sigma$) between σ_{max} (at T_{min}) and σ_{min} (at T_{max}) is comparable according to the two behavior laws. On the other hand, the two models are distinguished by the cyclic plastic deformation and the corresponding stress during the first heating. By taking into account the speed effects (viscosity), the EVP model allows a more realistic calculation where the plasticity and the stress are lower compared to what is given by the EP model. Furthermore, taking into account the cyclic softening resulting from the microstructural evolution of the steel results in an increase in the mean stress given by the EVP model, whereas in the EP model the threshold stresses (σ_{max} and σ_{min}) and therefore the mean stress remain unchanged over several cycles. If the life and/or crack propagation criteria are based on the stress amplitude, then the two constitutive laws lead to the same conclusions in our conditions. On the other hand, if these criteria use other components of the stress (maximum, minimum, or mean) or the plastic deformation, then the choice of the constitutive law can influence the results of the life prediction.

6. Bibliographic references

1. Medjedoub, F., Détermination des paramètres influant sur le phénomène d'endommagement par fatigue thermique des moules en fonderie sous pression d'aluminium. Thèse de doctorat à École des Mines de Paris, 2004.
2. Malm, S. et L. Norstrom, Material-related model for thermal fatigue applied to tool steels in hot-work applications. Metal Science, 1979, p. 544-550.
3. Daffos, C., Endommagement des outillages de forgeage traités par nitruration: Etude et Modélisation. Thèse de Doctorat à l'Institut National des Sciences Appliquées de Toulouse, 2004.
4. Velay, V., Modélisation du comportement cyclique et de la durée de vie d'aciers à outils martensitiques. Thèse Doctorat à l'École des Mines de Paris, 2003
5. Lemaitre, J. and J. Chaboche, Mécanique des Matériaux Solides. 1985.
6. Ahmer, Z., et al., Cyclic behaviour simulation of X38CRMOV5-47HRC (AISI H11)-tempered martensitic hotwork tool steel. International Journal of Microstructure and Materials Properties, 2008. 3(2): p. 326-335.
7. Zhang, Z., Modélisation du comportement cyclique anisotherme d'un acier martensitique 55NiCrMoV7 avec prise en compte du vieillissement. Thèse Doctorat à l'École des Mines d'Albi, 2002.
8. Delagnes, D., Comportement et tenue en fatigue isotherme d'aciers à outils Z38CDV5 autour de la transition oligocyclique-endurance. Thèse de Doctorat à l'Ecole des Mines de Paris, 1998.
9. Lemaitre, J. et Chaboche, JL., Mécanique des Matériaux Solides. Dunod,1985.
10. Barrau, O., Etude du frottement et de l'usure d'acier à outils de travail à chaud. Thèse Doctorat à l'Institut National Polytechnique de Toulouse, 2004.
11. Michaud, P., Influence des Éléments d'Alliages sur la Relation entre les Précipitations et les Propriétés Mécaniques Usuelles d'Acier à Outils à 5 % de Chrome. Thèse Doctorat à l'Ecole des Mines de Paris, 2006.
12. Oudin, A., Thermo-mechanical fatigue of hot-work tool steels. Thèse de Doctorat à l'École des Mines des Paris, 2001.
13. Policella, H. et P. Lesne. Crack initiation and propagation in thermal fatigue- Predictive modeling (Amorcage et propagation de fissures en fatigue thermique - Calculs de prévision). in Société Française de Métallurgie, Journées Internationales de Printemps sur la Fatigue à Haute Température, Paris, France, Juin 9-11, 1986. 1986.
14. Rezaï-Aria, F., Fatigue thermique et fatigue isotherme d'un superalliage à base de cobalt: étude métallurgique de l'endommagement et modélisation. Thèse de doctorat, Université de Paris-Sud, Centre d'Orsay, 1986.
15. Persson, A., S. Hogmark, and J. Bergström, Thermal fatigue cracking of surface engineered hot-work tool steels. Surface & Coatings Technology, 2005. 191(2-3): p. 216-227.
16. Orteu, J., et al., An Innovative Method for 3-D Shape, Strain and Temperature Full-Field Measurement Using a Single Type of Camera: Principle and Preliminary Results. Experimental Mechanics, 2008. 48(2): p. 163-179.
17. Lamesle, P., et al. Monitoring distorsions of metallic parts during quenching. in 5th International conference and european conference on heat treatment. 2007.
18. Ozisik, M., Heat transfer: a basic approach. 1985: McGraw-Hill Companies.
19. Dour, G., et al., Normalized thermal stresses analysis to design a thermal fatigue experiment. Journal of Thermal Stresses, 2004. 28(1): p. 1-16.

20. Ahmer, Z., et al., Cyclic behaviour simulation of X38CRMOV5-47HRC (AISI H11)-tempered martensitic hotwork tool steel. International Journal of Microstructure and Materials Properties, 2008. 3(2): p. 326-335.
21. Zhang, Z., Modélisation du comportement cyclique anisotherme d'un acier martensitique 55NiCrMoV7 avec prise en compte du vieillissement. Thèse Doctorat à l'École des Mines d'Albi, 2002.
22. Spera, D., What is Thermal Fatigue ?. Thermal Fatigue of Materials and Components, ASTM STP 612, 1976, p. 3-9.
23. Remy, L. Méthodologie de la fatique thermique. Journées Internationales de Printemps sur la Fatigue à Haute Température, Paris, France, Juin 9-11, 1986.